Nanoscale

PAPER

View Article Online
View Journal | View Issue

Cite this: *Nanoscale*, 2022, **14**, 17700

Anti-KIT DNA aptamer-conjugated porous silicon nanoparticles for the targeted detection of gastrointestinal stromal tumors†

Sanahan Vijayakumar,[a] Seyedmehdi H. Nasr,[b] Jacob E. Davis,[c,d] Edward Wang,[a] Jonathan M. Zuidema,[b,e] Yi-Sheng Lu,[a] Yu-Hwa Lo,[a,f] Jason K. Sicklick,[c,d,g] Michael J. Sailor *[a,b] and Partha Ray *[c,d]

Received 15th July 2022,
Accepted 8th November 2022

DOI: 10.1039/d2nr03905b

rsc.li/nanoscale

Evaluation of Gastrointestinal Stromal Tumors (GIST) during initial clinical staging, surgical intervention, and postoperative management can be challenging. Current imaging modalities (*e.g.*, PET and CT scans) lack sensitivity and specificity. Therefore, advanced clinical imaging modalities that can provide clinically relevant images with high resolution would improve diagnosis. KIT is a tyrosine kinase receptor over-expressed on GIST. Here, the application of a specific DNA aptamer targeting KIT, decorated onto a fluorescently labeled porous silicon nanoparticle (pSiNP), is used for the *in vitro* & *in vivo* imaging of GIST. This nanoparticle platform provides high-fidelity GIST imaging with minimal cellular toxicity. An *in vitro* analysis shows greater than 15-fold specific KIT protein targeting compared to the free KIT aptamer, while *in vivo* analyses of GIST-burdened mice that had been injected intravenously (IV) with aptamer-conjugated pSiNPs show extensive nanoparticle-to-tumor signal co-localization (>90% co-localization) compared to control particles. This provides an effective platform for which aptamer-conjugated pSiNP constructs can be used for the imaging of KIT-expressing cancers or for the targeted delivery of therapeutics.

Introduction

Gastrointestinal stromal tumor (GIST) is the most common sarcoma, with ~6000 new cases in the United States annually.[1] Conventional cross-sectional imaging techniques such as CT and MRI are routinely used to evaluate GIST and provide essential anatomic information for clinical staging and operative planning. Additional functional information is provided by [^{18}F] fluorodeoxyglucose positron emission tomography (PET),[2] which non-specifically identifies the areas with increased glucose metabolism in the context of tumors, infection, or inflammation. Unfortunately, these imaging modalities may fail to detect lesions or fail to differentiate GIST from benign tumors in the gastrointestinal tract, including schwannomas, leiomyomas, and pancreatic rests, leading to unnecessary biopsies and/or surgical resections. Therefore, non-invasive approaches with higher sensitivity and specificity are needed for: (1) initial radiological staging to identify subtle but clinically relevant metastases; (2) improved recurrence detection after tumor resection; (3) the assessment of treatment responses in the neoadjuvant (*i.e.*, preoperative) and metastatic settings, and (4) distinguishing GIST from other tumors that radiologically mimic GIST. To date, no such approach exists for the care of these patients.

GIST is diagnosed by overexpression of KIT, a receptor tyrosine kinase. Furthermore, approximately 60–70% of GIST are driven by oncogenic KIT gene mutations.[3,4] The treatment of GIST provided the first proof of principle for precision medicine in solid tumors as driver mutations in the KIT gene was identified and effectively targeted with imatinib (IM; Gleevec,

[a]*Materials Science and Engineering Program, University of California, San Diego, La Jolla, California, 92093, USA. E-mail: msailor@ucsd.edu*
[b]*Department of Chemistry & Biochemistry, University of California, San Diego, La Jolla, California, 92093, USA*
[c]*Department of Surgery, Division of Surgical Oncology, University of California, San Diego, San Diego, California, 92093, USA. E-mail: pray@health.ucsd.edu*
[d]*Moores Cancer Center, University of California, San Diego, La Jolla, California, 92093, USA*
[e]*Department of Neurosciences, University of California, San Diego, San Diego, California, 92093, USA*
[f]*Department of Electrical & Computer Engineering, University of California, San Diego, La Jolla, California, 92093, USA*
[g]*Department of Pharmacology, University of California, San Diego, San Diego, California, 92093, USA*

†Electronic supplementary information (ESI) available: N2 adsorption/desorption isotherm data, DLS and ζ-potential data of nanoparticle constructs, FTIR spectra of constructs, fluorescence measurements of dye-conjugated particles, standard curve of dye-labeled aptamer, TGA measurements of particle constructs, HMC-1.2 cell line *in vitro* targeting data, temporal *in vivo* IVIS imaging of mice, biosafety, and histopathological analysis of pSiNP constructs. See DOI: https://doi.org/10.1039/d2nr03905b

Novartis, Basel, Switzerland), a tyrosine kinase inhibitor (TKI). However, IM does not cure GIST. Therefore, R0 resection (*i.e.*, tumor-free margins) is the mainstay of curative treatment. Nevertheless, the risk of metastatic disease is substantial even in cases where tumor-free margins are achieved. The metastases frequently involve the peritoneal surfaces and/or liver due to peritoneal seeding and hematogenous spread, respectively. Therefore, methods to improve visualization of metastases may be advantageous for more accurate radiographic staging and treatment decision-making for patients with GIST.[5]

Currently, GIST diagnosis relies on analyzing tissue procured from either biopsy or surgical specimens. Although KIT-expressing GISTs are effectively diagnosed with immunohistochemical staining with anti-KIT antibodies, this approach requires maintaining hybridomas for production, which is expensive and time-consuming. Aptamers are a promising alternative to antibodies as a targeting species. Aptamers are single-stranded (ss) oligonucleotide (ssDNA or ssRNA) ligands that are selected against specific cell or protein targets through SELEX (Systematic Evolution of Ligands by Exponential Enrichment), an *in vitro* iterative process.[6,7] Aptamers assume their structure through intra-molecular base-pairing between complementary nucleotides, and they assume secondary, then tertiary structures. These complex DNA structures can bind to their cognate targets with high affinity and specificity, with binding constants comparable to monoclonal antibodies. Due to their small size, aptamers have shown greater tissue penetration in comparison to antibodies, as well as non-immunogenic. Aptamers are also amenable to various chemical modifications, including conjugation with compounds such as fluorophores or drugs. Thus, modified aptamers have been proposed for several applications, including *in vitro* and *in vivo* imaging, as well as targeted drug delivery.[8,9]

Recently we published the first report to employ an anti-KIT aptamer for targeted labeling of GIST. We demonstrated that the aptamer bound to cancer cells in a KIT-dependent manner and was highly specific for GIST cell labelling *in vitro*. Functionally, the KIT aptamer bound extracellular KIT in a manner similar to KIT monoclonal antibody staining and was trafficked intracellularly *in vitro*. The KIT aptamer bound dissociated primary human GIST cells. Additionally, the KIT aptamer specifically labeled intact human GIST tissue *ex vivo*, as well as peritoneal xenografts in mice with high sensitivity. These results represented the first application of an anti-KIT DNA aptamer-based method for targeted detection of GIST *in vitro* and *in vivo.*[10] However, the system needed improvement in two aspects in order to enable translation. These included increasing the binding affinity of the aptamer and improving the ability to detect this binding in a fashion that is amenable to intraoperative monitoring.

Traditional imaging approaches such as Computed Tomography (CT) or Magnetic Resonance Imaging (MRI), and Positron Emission Tomography (PET) routinely fail to detect lesions, clinically relevant metastases or to differentiate GIST from benign tumors leading to unnecessary biopsies and surgical resections.[5,10,11] Fluorescence-based approaches provide essential anatomic information for surgeons regarding clinical staging and operative planning, though they require a substantially high concentration of imaging agents and fluorescent probes, bringing the added disadvantage that they can be easily photobleached.[12–14] Nanoparticles can overcome these issues by providing a vehicle in which a considerable concentration of imaging agent can be entrapped, which serves to protect the fluorescent payload from photobleaching while increasing its circulation time throughout the body until it reaches its target.[12,14]

A challenge with GIST is the formation of metastases that are commonly associated with drainage tissues. It has been previously demonstrated that nanoparticle complexes are cleared by the renal system and/or the reticuloendothelial system (RES), including the liver, spleen, and lungs. Being able to specifically target metastatic regions while limiting non-specific endocytotic uptake by healthy cells and macrophages is a major challenge. Recent work has shown the effective use of nanoparticles for the imaging of GIST through MRI, and near-IR fluorescence.[11] However, these ultra-small (<10 nm) nanoparticle complexes utilized the EPR effect to localize to the GIST tumors. Despite this promising work, relying on the EPR effect for targeting has been shown to be less effective than specific receptor targeting.[15–21]

The combination of targeting moieties and nanoparticles has been shown to be an effective platform for targeting tumors and other hard-to-reach organs. Nanoparticles provide an enhanced surface area in which multiple copies of a targeting moiety, such as monoclonal antibodies, peptides, or aptamers, can be conjugated onto a single carrier, enhancing its specific targeting capabilities by providing multiple orientations in which the carrier could bind to the tumor receptor.[19,20] Compared to free targeting counterparts, recent literature has shown up to a 30- to 40-fold greater targeting efficacy for nanosystems conjugated with targeting moieties.[15,17,19,20] A wide range of nanocarriers are of interest, ranging from lipids and polymers to metallic particles. Porous silicon nanomaterials have been used extensively for the imaging and treatment of cancers due to their low-toxicity degradation pathway (that yields silicic acid end products which are readily excreted from the body), surface chemistry, and their tunable mesoporous features.[13,15,17,18,22] Porous silicon nanoparticles (pSiNP) have been previously used for the specific targeting of tumors with the surface-conjugation of peptides, antibodies, and aptamers, and they have been used as a delivery vehicle for biological payloads and imaging agents, due to their large open pore volumes (typically 50–80%).[13,14,16,17,23–25]

This study was designed to develop a simple nanoparticle imaging construct that can be injected intravenously (IV) into GIST-burdened mice. Therefore, in this context, a porous silicon nanoparticle (pSiNP) would provide an attractive delivery platform due to the many tunable pore characteristics that can be used to load imaging agents, while it's very versatile surface chemistry can enable specific functionalization of targeting moieties. Utilizing *in vitro* experiments with KIT-expres-

sing cells, we demonstrated the enhanced multivalency effects of an aptamer-grafted nanoparticle compared to free KIT aptamers and KIT mAb. We reasoned that, by conjugating this aptamer onto a nanoparticle construct, its binding affinity can be increased by conjugating multiple aptamer-ligands onto a single particle.[19] We subsequently used human GIST-injected mice for the *in vivo* labelling of GIST, isolating GIST liver metastases, and assessing tumor co-localization. We found that the KIT-aptamer conjugated pSiNPs can detect GIST cells with high affinity showing greater than 90% of tumor co-localization of visible metastases of nanoparticle to tumor signals within harvested *ex vivo* IVIS images of organs and fluorescence images of GIST-burdened liver sections when assessed through ImageJ. This study provided the first proof of principle that anti-KIT DNA aptamers conjugated onto pSiNPs can be a platform for the targeted imaging of GIST, which has implications for the targeted imaging and delivery of therapeutics for other KIT-expressing cancers.

Results and discussion

Development of aptamer-conjugated nanoparticles

The porous silicon nanoparticles (pSiNPs) were prepared as previously described.[26] The as-formed nanoparticles displayed an average hydrodynamic diameter of 156 ± 20 nm, as measured by dynamic light scattering (DLS). The specific surface area was 333 ± 14.71 $m^2\ g^{-1}$, the pore volume 1.38 ± 0.08 $cm^3\ g^{-1}$ and the average pore size was 15 ± 0.13 nm, as determined from N_2 adsorption/desorption isotherms using the Brunauer–Emmett–Teller (BET) and Barrett–Joyner–Halenda (BJH) models (Fig. 2c & Table S1, ESI†). The nanoparticles were functionalized with heterocyclic-silanes (known as pSiNP-NH_2) and conjugated with fluorescent imaging labels Cy5.5 or fluorescein isothiocyanate (referred to here as pSiNP-NH_2-Cy5.5 or pSiNP-NH_2-FITC, respectively) onto the amine-terminated surface. The particles were subsequently PEGlyated with a bifunctional PEG linker (referred to here as pSiNP-NH_2-Cy5.5-PEG or pSiNP-NH_2-FITC-PEG, respectively). These multiple processes provided a slight increase in the hydrodynamic diameter and changes in pore size and pore volume (Fig. 2d & Table S2, ESI†).

The final nanoparticle construct had a coating of polyethylene glycol (PEG) with a functional tail that was used to attach the aptamer. The PEG coating was attached to the pSiNPs through the addition of a cyclic azasilane reagent (DMDASCO, 2,2-dimethoxy-1,6-diaza-2-silacyclooctane), which was used to functionalize primary amine groups easily and rapidly onto the pSiNP surface *via* a ring-opening click reaction (Fig. 1a).[8] The successful functionalization of the silane was confirmed through Fourier transform infrared (FTIR) spectroscopy, dynamic light scattering (DLS) and ζ-potential measurements, indicating both N–H stretching and bending modes an increase in size and positive surface charge values (+18 ± 4 mV) (Table S2, ESI†). Both the positive charge and the amine terminal groups enabled a reactive surface for NHS ester-terminated fluorophores to be grafted to the particle (Fig. S1, ESI†). This yielded a slight change in the ζ-potential measurements, but an increase in the particles' fluorescence for both Cy5.5 and FITC dyes (Table S2, Fig. S2 & Fig. S4, ESI†). The remain-

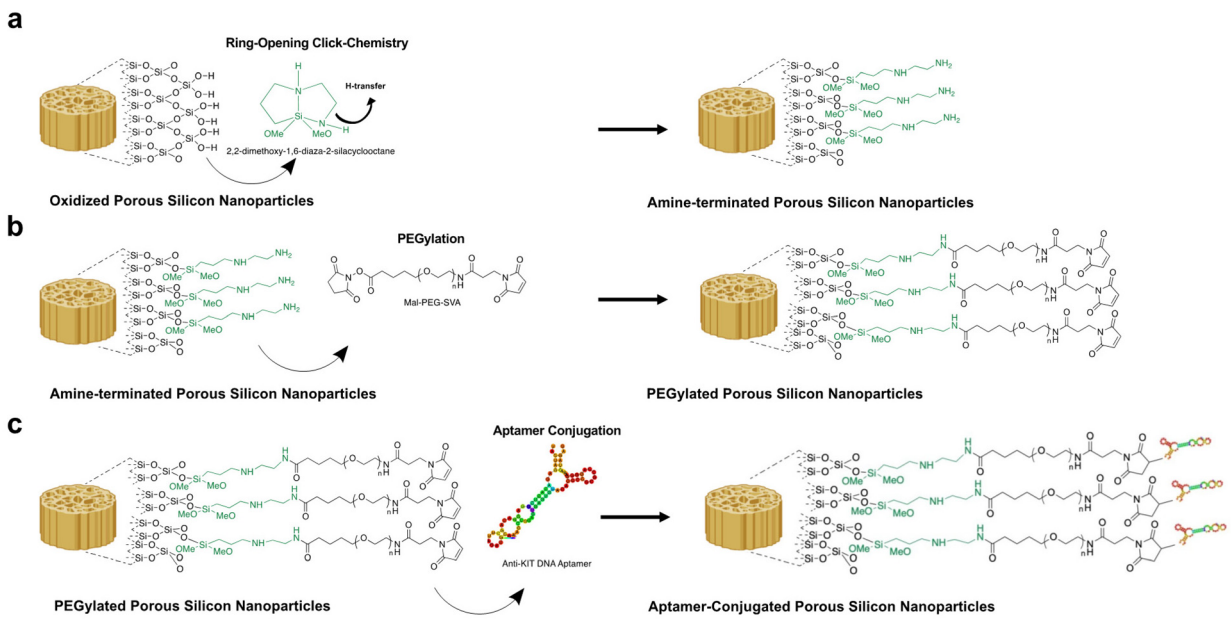

Fig. 1 Preparation of silane-modified pSiNPs for the attachment of PEG and aptamers. (a) Schematic illustration of the ring-opening procedure to functionalize pSiNPs with primary amines for the attachment of PEG. (b) Schematic illustration of the attachment of Mal-PEG-SVA to enable circulation of the particles *in vivo* while also providing a surface for which the aptamer ligands could bind to the particle. (c) Schematic illustration of the KIT aptamer attachment. The SH- terminated aptamers bind covalently to the maleimide-terminated PEG on the pSiNPs through sulfhydryl- maleimide coupling.

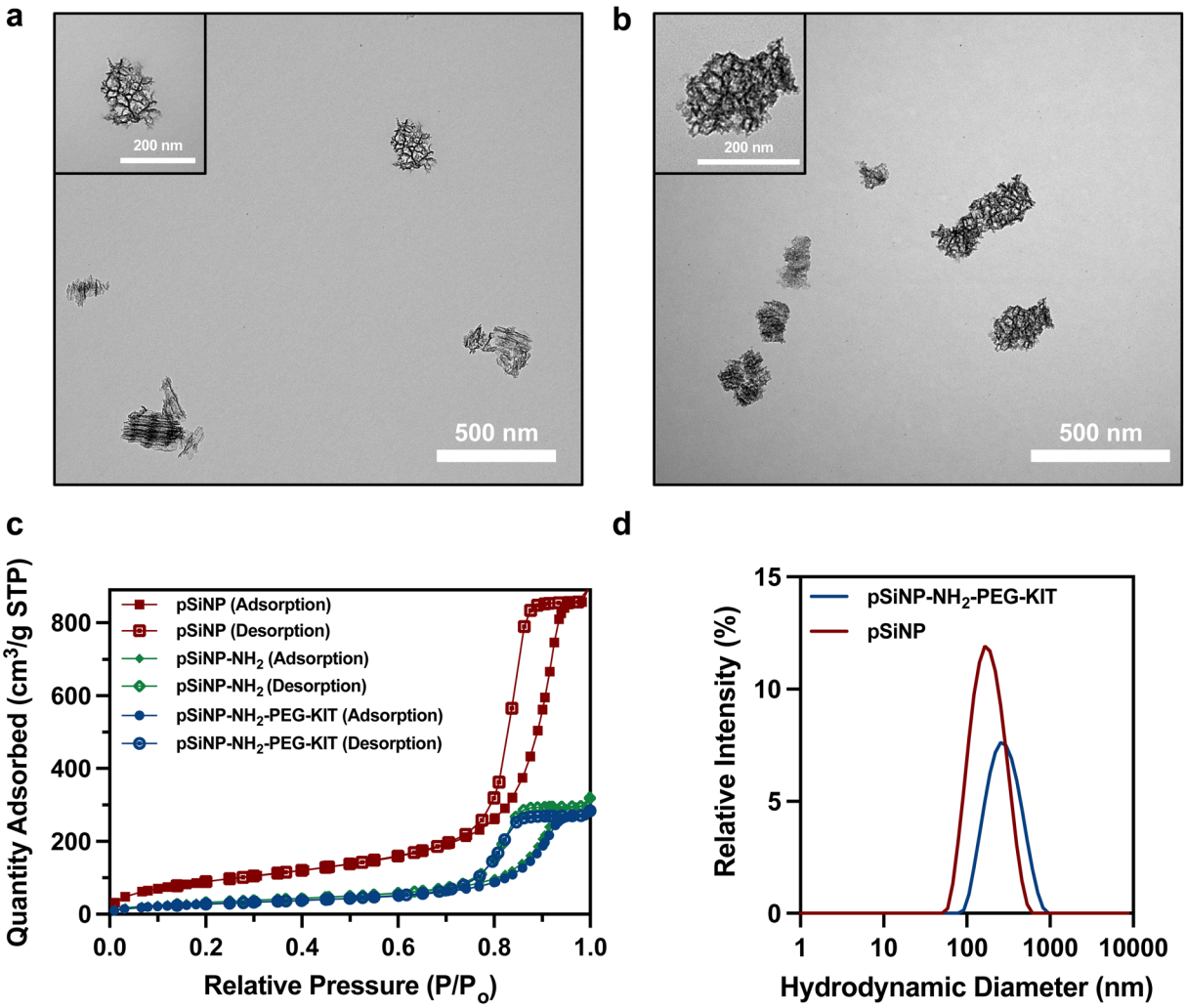

Fig. 2 KIT-Aptamer conjugated porous silicon nanoparticles (KIT-pSiNP). Transmission Electron Microscopy (TEM) images of (a) freshly etched and (b) aptamer-conjugated particles (scale bar = 500 nm); the insert shows a closer view of a single nanoparticle (scale bar = 200 nm). (c) N_2 adsorption–desorption isotherms of the empty, unmodified pSiNPs, silane-functionalized pSiNPs and aptamer-conjugated, PEGylated pSiNPs. The isotherms are used to determine the pore size and pore volume of the particles. (d) Dynamic light scattering (DLS) data of freshly etched pSiNPs and PEGylated and aptamer-conjugated particles. There is an increase in hydrodynamic size due to the surface functionalization, PEGylation and aptamer conjugation of the particles.

ing primary amine groups were used to graft PEG chains to the particle surface. A specialized PEG, maleimide-PEG-succinimidyl valerate (MAL-PEG-SVA) was utilized as a protective overcoat for the particles. This PEG formed amide bonds between the succinimidyl valerate and the surface primary amine groups of the pSiNPs, leaving a free maleimide group at the terminal end, used for aptamer attachment. The functionalization of the PEG group was also confirmed through FTIR spectroscopy and DLS measurements, yielding an increase in the hydrodynamic size and functional groups of strong aliphatic C–H stretching and amide C═O stretching bands (Table S2 & Fig. S2b, ESI†). The KIT aptamer was subsequently grafted onto the nanoparticle using the terminal maleimide groups from the PEG (Fig. 1c). The aptamer, with a thiol termination, was grafted using the commonly used sulfhydryl-maleimide reactive crosslinker coupling to form a covalent thioether bond (known as pSiNP-NH_2-Cy5.5-PEG-KIT or pSiNP-NH_2-FITC-PEG-KIT). Due to the presence of negatively charged aptamer ligands on the nanoparticles surface, the ζ-potential measurement decreased in value to +2.33 ± 1.02 mV (Table S2, ESI†). Aptamers grafted to the pSiNP surface were also confirmed using FITC-labelled aptamers, with a 6-FAM label conjugated to the 3′ end of the aptamer. By measurement of the optical absorbance of the supernatant (λ = 520), the amount of aptamer on the surface was found to be 32.52 ± 3.23 nmol mg^{-1} pSiNP (n = 3), which corresponds to a yield of 81.3% of the added aptamer that became bound to the pSiNP surface (Fig. S5, ESI†). Similarly, thermogravimetric analysis (TGA) measurements were used to assess the PEG surface coverage (Fig. S6, ESI†).

***In vitro* cellular targeting.** Cellular targeting and imaging properties of the pSiNPs were screened using two cancer cell

lines that overexpress KIT receptors, HMC-1.2 (Mastocytosis) and GIST-T1 (Gastrointestinal stromal tumor) as a preliminary model. We wanted to determine the specificity of the anti-KIT aptamer, conjugated to pSiNPs to bind to cells in a KIT-dependent manner. Initially, ssDNA KIT aptamers were obtained from previously published literature (5′-GAGGCATACCAGC TTATTCAAGGGGCCGGGGCAAGGGGGGGGTACCGTGGTAGGA CATAGTAAGTGCAATCTGCGAA-3′).[10] In addition, a scrambled aptamer sequence was generated through a random oligonucleotide sequence generator, with the same free energy of the specific KIT aptamer sequence. The scramble sequence is as follows: (5′-TGACGGGAGACTTAAAACGCAAGGGGTGCAGCTA TCGCGGAGGCCAAGGGTTCAAGTCGACGGGTAGCTA- GGTTGG A-3′; Oligo Calculator version 3.27, biotools.nubic.- northwestern.edu). Both the aptamer and scramble sequences were synthesized with a thiol modification on the 5′ end and both an unmodified sequence and a 6-FAM fluorophore modification on the 3′ end (Integrated DNA Technologies) for the various experimental applications. Though this KIT aptamer has previously displayed tumor-targeting properties, they have not been used as an active ligand mounted on pSiNPs targeting GIST cancers. For comparison, we have included in our experimental controls the scramble aptamer target to measure specificity as well as free aptamer targets and a KIT-specific monoclonal antibody (mAb) as controls to measure multivalency effects of aptamer-conjugated pSiNP constructs as compared to free aptamer ligands and KIT mAb. Following the conjugation procedure, scramble aptamers were bound to the fluorophore-labelled nanoparticles, while equivalent concentrations of free aptamer, anti-KIT specific and scramble, were used as individual controls. In addition, an anti-KIT mAb was used as another positive control to compare the binding of the KIT aptamer conjugated particles. Both HMC-1.2 and GIST-T1 cells were incubated with either the aptamer–nanoparticle constructs containing the KIT aptamer (pSiNP-NH_2-FITC-PEG-KIT) a negative control scramble aptamer that is not specific to GIST (pSiNP-NH_2-FITC-PEG-SCR) a non-aptamer containing nanoparticle (pSiNP-NH_2-FITC-PEG), free aptamers (KIT-6-FAM & SCR-6-FAM), and antibody (KIT mAb) to confirm the intracellular localization of the labelled particles and aptamers after 1 hour and were subsequently quantified by flow cytometry (Fig. 3a & Fig. S5, ESI†). Confocal micrographs were subsequently taken of the nanoparticle constructs and were consistent with the nanoparticle cellular uptake of the pSiNP-NH_2-FITC-PEG-KIT particles (Fig. 3b). The significant difference of the FL1-A Fluorescence geometric mean (GM) of pSiNP-NH_2-FITC-PEG-KIT particles compared to the scramble-aptamer and non-aptamer conjugated pSiNP controls show that the pSiNP-NH_2-FITC-PEG-KIT are specific to both GIST-T1 (12.83-fold binding increase than pSiNP-NH_2-FITC-PEG-SCR & 12.92-fold binding increase than pSiNP-NH_2-FITC-PEG) and HMC-1.2 cell lines (17.41-fold binding increase than pSiNP-NH_2-FITC-PEG-SCR & 27.48-fold binding increase than pSiNP-NH_2-FITC-PEG). Compared to free KIT aptamers and a KIT mAb, the pSiNP-NH_2-FITC-PEG-KIT constructs showed a 5.24- and 5.64-fold binding increase for GIST-T1 cells and 5.39- and 5.70-fold increase with HMC-1.2 cells respectively (Fig. 3a & Fig. S7a, ESI†) Due to the results of these experiments, we decided to go forth with *in vivo* studies.

***In vivo* & *ex vivo* cellular targeting of nanoparticles.** We next investigated the *in vivo* binding and localization of KIT-Aptamer conjugated particles and control nanoparticles. Following previously developed intrasplenic GIST-T1 models, we examined pSiNP-NH_2-Cy5.5-PEG-KIT binding to the tumors.[5,10,27–29] GIST-T1-GFP cells, co-injected with cancer associated fibroblasts (CAFs) were used in this model to visualize the tumor burden. We previously demonstrated that in the spleen-to-liver-GIST metastasis model used here, the CAFs can

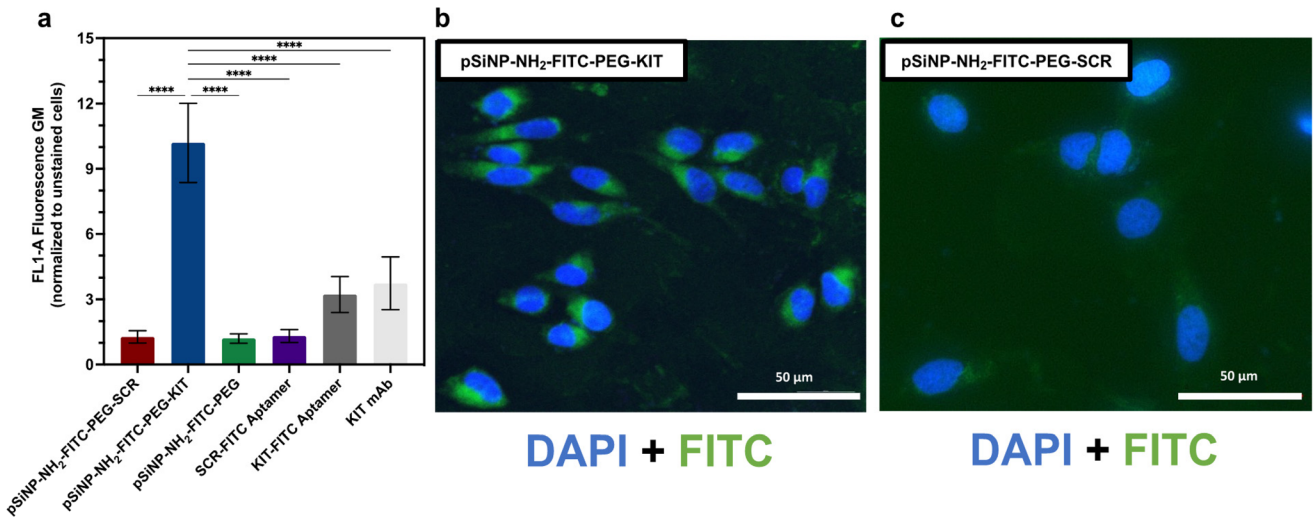

Fig. 3 Investigation of cellular targeting of pSiNP constructs in a model GIST-T1 cancer cell line. (a) Interaction of GIST-T1 cells with pSiNP constructs quantified by flow cytometry (mean value ± SD, n = 3, ****p < 0.0001). Confocal microscopy images of GIST-T1 cells incubated with (b) pSiNP-NH_2-FITC-PEG-KIT constructs and (c) pSiNP-NH_2-FITC-PEG-SCR. Both images are merged laser lines for DAPI and FITC (scale bar = 50 μm).

accelerate GIST growth and metastasis.[30] Three weeks after intrasplenic injection, mice underwent tail-vein injection of either pSiNP-NH_2-Cy5.5-PEG-KIT, pSiNP-NH_2-Cy5.5-PEG-SCR or pSiNP-NH_2-Cy5.5-PEG constructs at a concentration of 10 mg kg^{-1}. Binding of the constructs were assessed every hour for 5 hours, based on the intensity of the GIST-T1-GFP and Cy5.5 signals for each mouse, using IVIS (*In vivo* Imaging System) (Fig. S8 & S9a, ESI†). It is seen that the mean signal intensities of pSiNP-NH_2-Cy5.5-PEG-SCR and pSiNP-NH_2-Cy5.5-PEG were lower than that of pSiNP-NH_2-Cy5.5-PEG-KIT signals. After 5 hours, the Cy5.5 intensities of all the pSiNP constructs were assessed to identify the greatest signal within the abdomen (Fig. 4). As pSiNP-NH_2-Cy5.5-PEG-KIT constructs selectively bind to GIST-T1 tumors, any non-specific particle constructs, pSiNP-NH_2-Cy5.5-PEG-SCR and pSiNP-NH_2-Cy5.5-PEG, would be cleared out from the mice much more rapidly. However, the slightly greater positive charge of pSiNP-NH_2-Cy5.5-PEG particles (Fig. S2a, ESI†) is shown to have lower clearance than the pSiNP-NH_2-Cy5.5-PEG-SCR and follows the behavior of positively charged particles in tumors shown in literature.[31,32] Collectively, all these measurements suggest that the scrambled pSiNP-NH_2-Cy5.5-PEG-SCR and pSiNP-NH_2-Cy5.5-PEG constructs are non-selective due to their faster clearance from these RES tissues, while the pSiNP-NH_2-Cy5.5-PEG-KIT had increased tumor detection due to the strong signal intensities at the multifocal disease sites.

We next evaluated the biodistribution of the nanoparticle constructs within our tumor-bearing mice. Analysis of the specific binding to these tumors were done by harvesting the organs of the liver, spleen and kidneys after 5 hours post nanoparticle injection, for what we have named as *ex vivo* imaging for this study. Separately, the organs were imaged *ex vivo* by IVIS to isolate for the GIST-T1 metastases using a GFP signal. As GFP is generally difficult to image by IVIS, due to both tissue autofluorescence and lack of depth penetration from the IVIS laser,[33,34] the *ex vivo* images of the liver, spleen and kidneys would provide adequate evidence of the tumor model and an effective means to calculate nanoparticle-to-tumor co-localization. Subsequently, the Cy5.5 signal from the administered particles were also measured. Both signals were subsequently merged to isolate for the signal overlap. This step was repeated for all sets of particle constructs (Fig. 5a). The merged GFP and Cy5.5 signal images were then assessed using ImageJ to analyze the signal overlap, known as GFP co-localization (%), to quantify the binding effectiveness of the pSiNP-NH_2-Cy5.5-PEG-KIT constructs towards GIST metastases (Fig. 5b & c). The importance of calculating the GFP co-localization is that our GIST model metastasizes within organs that are part of the reticuloendothelial system (RES) and mononuclear phagocyte system (MPS). As nanoparticles are cleared by phagocytes; hepatic clearance by Kupffer cells within the liver and the spleen, and renal clearance by the kidneys, the importance of specific binding to GIST-T1 metastases that occur within these regions is paramount due to the potential of non-specific uptake in these organs. Active-targeted pSiNPs bearing KIT-specific aptamers will bind to and be internalized by these solid tumors, while non-active-targeted nanoparticles will be distributed within these organs non-specifically. Biodistribution of the particles towards other organs was not studied due to the GIST-T1 tumor model affecting only the

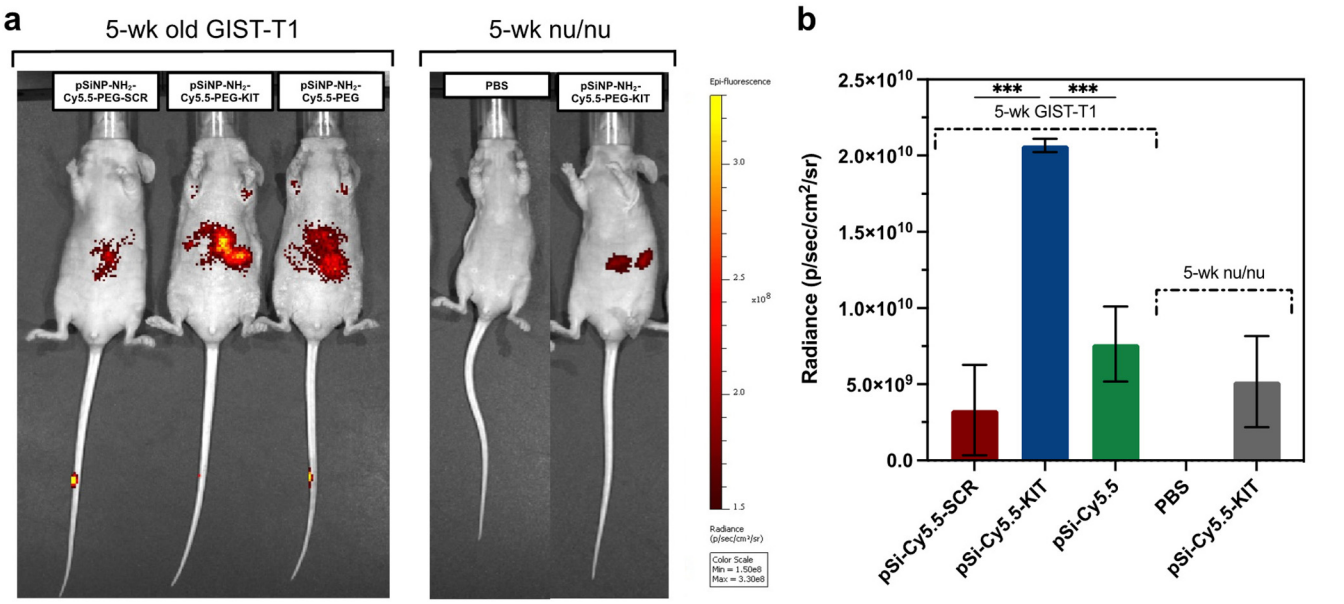

Fig. 4 *In vivo* evaluation of targeted pSiNP constructs in GIST-T1 model. (a) IVIS images of both 5-week-old GIST-T1 and 5-week-old nu/nu mice injected with pSiNP constructs tail-vein. Cy5.5 signals, from fluorophores attached onto the pSiNP constructs were isolated within abdomen regions after 5 hours. (b) The IVIS signals were quantified for different construct groups indicating that injection of pSiNP-NH_2-Cy5.5-PEG-KIT particles produces the highest radiance signal (mean value ± SD, n = 3, ***p < 0.001).

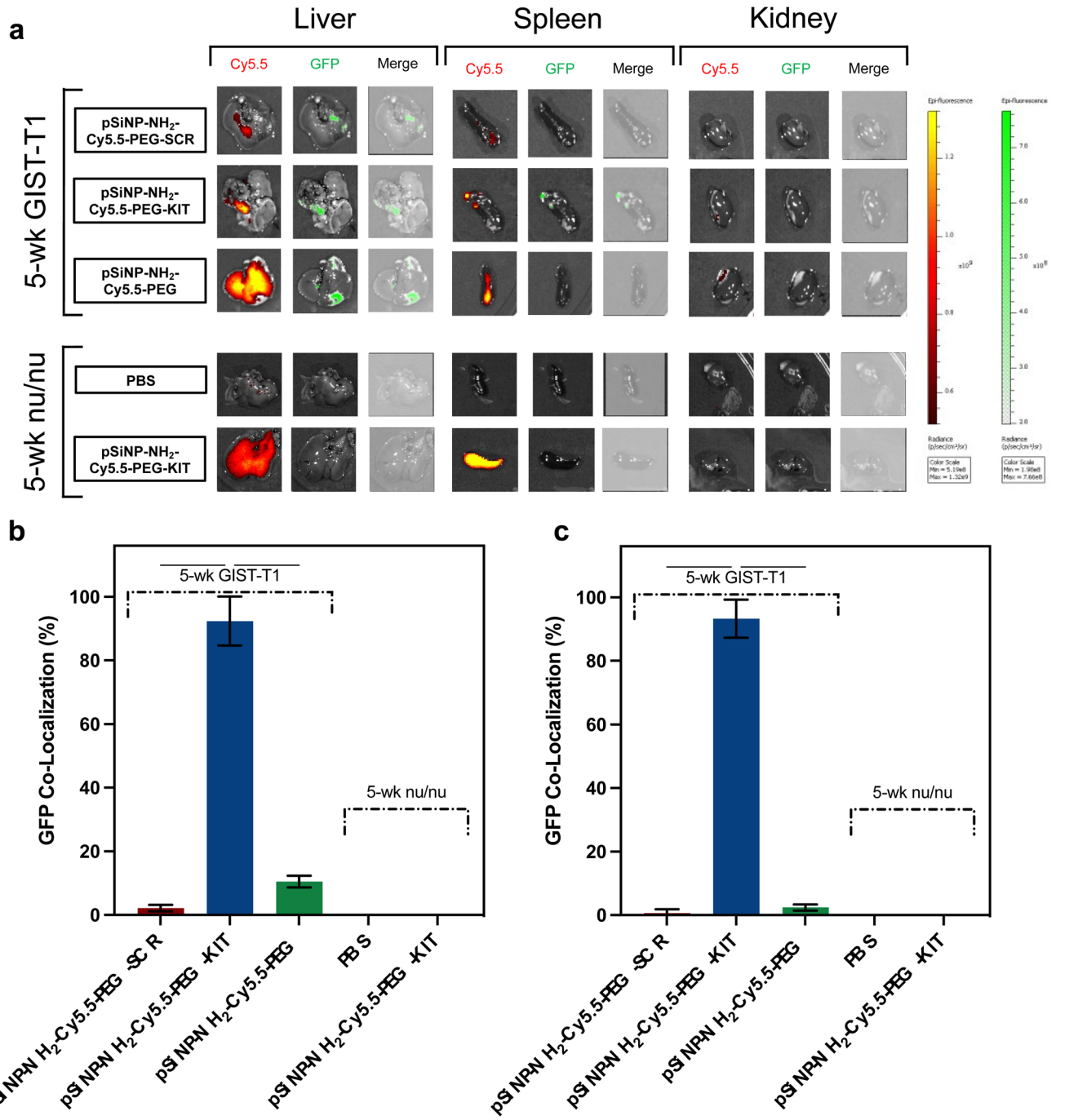

Fig. 5 *Ex vivo* imaging of abdominal organs following injection of different pSiNP constructs. (a) IVIS images of harvested liver, spleen, and kidneys of GIST-T1 tumor burden and nu/nu mice. Cy5.5 signals from the injected pSiNP constructs and GFP signals from the GIST-T1-GFP metastases were imaged, and the signals were merged. GIST-T1-GFP co-localization for pSiNP constructs as assessed by ImageJ for (b) the liver (mean value ± SD, n = 3,****p < 0.0001) and (c) spleen for GIST-T1 tumor burden and nu/nu mice (mean value ± SD, n = 3,****p < 0.0001). Kidneys were not assessed for co-localization as no visible GFP signal was measured in any of the mice.

liver and the spleen in this intrasplenic GIST-metastasis model, however the general biodistribution of pSiNPs have been previously studied extensively.[15–17,35] The calculation of GFP co-localization will provide a quantitative measure of nanoparticle specificity (pSiNP-NH_2-Cy5.5-PEG-KIT) *versus* other non-GIST-specific nanoparticle controls (pSiNP-NH_2-Cy5.5-PEG-SCR and pSiNP-NH_2-Cy5.5-PEG), especially due to the significant internalization of the non-specific pSiNP-NH_2-Cy5.5-PEG particles throughout the liver and spleen, but not within the tumor-specific regions. Through ImageJ, the specificity of pSiNP-NH_2-Cy5.5-PEG-KIT particles is significant, with greater than 90% in tumor co-localization for both the liver

and spleen (mean value ± SD, n = 3, $*p < 0.05$) while pSiNP-NH_2-Cy5.5-PEG-SCR and pSiNP-NH_2-Cy5.5-PEG controls yield very little specific uptake (15%> co-localization) due to its random distribution within the liver and spleen. From Fig. 5a, there is no visible GIST metastases within the kidneys as well as a significantly lower nanoparticle distribution. The lack of GFP signal limited the quantification of pSiNP to GFP co-localization within this organ.

Due to the significantly high GFP signal in the liver and the distribution of pSiNP constructs within the liver, further *ex vivo* analysis was undertaken to assess the specificity of the pSiNP-NH_2-Cy5.5-PEG-KIT constructs towards GIST tumors internalized within the organ. Fluorescence images of frozen liver sections were used to assess the specific targeting properties of the constructs when internalized within the liver in addition to assessing GIST metastases not visible on the liver surface (Fig. 6a). As a control, frozen liver sections of healthy 5-week-old nu/nu mice were also imaged. This was done to confirm the lack of GFP signal within healthy mice as well as to assess the internalization and distribution of pSiNP-NH_2-Cy5.5-PEG-KIT within the liver due to RES clearance. Both Cy5.5 and GFP signals from the pSiNP constructs and the GIST-T1-GFP tumor metastases, respectively, were merged, and GFP co-localization was used to quantify the KIT labelling to GIST (Fig. 6b). Once again, there is significantly greater co-localization of the pSiNP-NH_2-Cy5.5-PEG-KIT constructs than both pSiNP-NH_2-Cy5.5-PEG-SCR and pSiNP-NH_2-Cy5.5-PEG particles (mean value ± SD, n = 5, $p < 0.05$). Within the healthy control group, there is Cy5.5 signal due to pSiNP-NH_2-Cy5.5-PEG-KIT accumulation, which is also seen in Fig. 5a. Similar to the *ex vivo* IVIS images of the harvested organs, there is some slight GFP co-localization from the control pSiNP-NH_2-Cy5.5-PEG constructs due to the non-specific uptake of the particles. These results, combined with Fig. 5, are consistent with the ability of the aptamer-conjugated particles to home to tumor cells within the RES- and MPS-related clearance organs, and the active targeting properties are consistent within the literature of similar pSiNP constructs that utilize peptide- and antibody-based targeting systems for other tumor models.[15,17,19]

Biosafety of nanoparticles

Prior to the incubation of pSiNPs for *in vivo* imaging experiments, we assessed the cell cytotoxicity and histological evaluations of major organs to analyze the short-term biosafety of the pSiNPs, cyclic-silane functionalization chemistry, the PEG overcoat, as well as the aptamer targeting moiety. Though we and others have previously shown that pSiNPs have yielded limited toxicity towards the liver, spleen and kidneys even after 4 weeks of nanoparticle injection,[36,37] the primary concern with the pSiNP construct was the heterocyclic silane chemistry which may induce a level of toxicity towards healthy cells. Though effective chemistry to amminate nanoparticles, this cyclic-silane has had limited use for both *in vitro* and *in vivo* experiments. For *in vitro* biosafety analysis, RAW 264.7 macrophage cell lines were incubated for 48 h with pSiNP formulations containing from 0.03125 mg to 0.5 mg of nanoparticles by total mass as well as a range of 1–16 ng of aptamer and an estimated 0.62–9.90 μg of azasilane reagent. These incubation concentrations were selected to cover a range of masses of nanoparticles injected *in vivo* at a concentration of 10 mg kg^{-1} per mouse. A CCK8/WST-8 assay was used to determine cell viability, and results indicated >95% for all pSiNP constructs compared to the media-treated control (Fig. S10a, ESI†). To

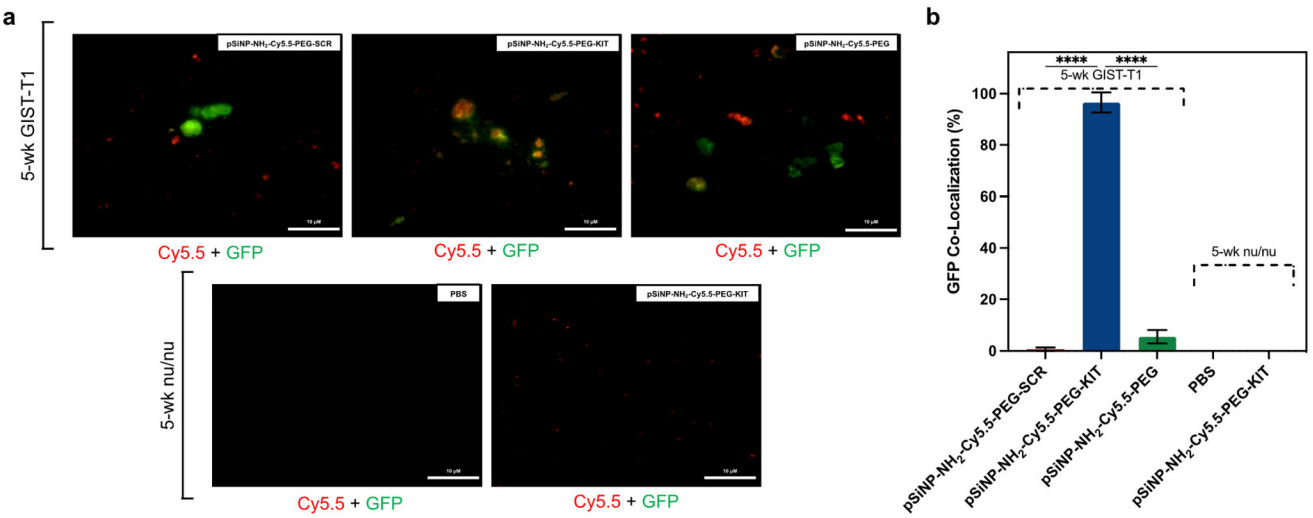

Fig. 6 *Ex vivo* imaging of frozen liver tissues. (a) Fluorescence images of frozen liver sections with merged Cy5.5 (red) and GFP (green) signals of GIST-T1 model containing metastasis that were sectioned and imaged by confocal microscopy (scale bar = 10 μm). Frozen liver tissues of 5-week-old nu/nu mice were also imaged as a control to assess the distribution of pSiNP-NH_2-Cy5.5-PEG-KIT particles within the liver. Targeted KIT-aptamer conjugated pSiNPs showed an overlay of GFP and Cy5.5 signals confirming the presence of targeted pSiNPs within the metastasis tissues. (b) ImageJ was used to quantify the sliced samples for the GFP co-localization of the various pSiNP constructs (mean value ± SD, n = 5, $****p < 0.0001$).

test short-term *in vivo* biosafety, healthy 5- to 6-week-old nu/nu mice were injected tail-vein with the pSiNP-NH_2-Cy5.5-PEG-KIT constructs at doses corresponding to 10 mg kg^{-1} of pSiNP and ~32 ng mg^{-1} pSiNP of aptamer and 198 μg mg^{-1} pSiNP of silane. After 5 h of nanoparticle injection, the major organs of interest, the liver, spleen, and kidneys, were harvested and sectioned for hematoxylin and eosin (H&E) histopathological evaluation (Fig. 7). This timeframe was chosen to ensure that the nanoparticles showed no toxicity within the selected imaging timeframe of 5 hours, which corresponded to the optimal Cy5.5 signal window and nanoparticle clearance after *in vivo* injection. All major organs were found to show no histopathological findings (Table S3, ESI†). In addition, the possibility of nanoparticle toxicity was assessed using an Alanine aminotransferase (ALT) assay, which was used to measure the pyruvate activity generated due to nanoparticle accumulation within the liver, where an increased pyruvate generation is generally associated with liver toxicity (Fig. S10b and c, ESI†). Blood serum was collected from *in vivo* histological experiments and following protocols from an ALT assay kit (Sigma), pSiNP-NH_2-Cy5.5-PEG-KIT constructs were compared to PBS-injected controls. It was found that pyruvate levels were equivalent for both pSiNP injections and PBS controls (Fig. S10c, ESI†), thereby indicating limited toxicity towards the liver.

Using nanoparticles for imaging or therapy of GIST has caught the attention of researchers recently. For instance, ultra-small (<10 nm), renal-clearable zwitterionic organic nanocarriers were used for image-guided surgery. In another study microRNA (miRNA) was formulated in a polymeric nanoparticle (~110 nm) to control the KIT expression. Although this work highlights the importance of KIT expression in management and therapy of GIST tumor, further animal studies are needed to evaluate the *in vivo* efficacy of the proposed formulation.[11,38] Both strategies have yielded very promising data and have shown that these platforms can reach GIST targets with high affinity. In both cases, however, the particles rely on passive targeting effects, either through retained circulation throughout the body or the enhanced permeability and retention (EPR) effect, to reach the GIST target. To the best of our knowledge, only one group has utilized an active-targeting strategy with emulsion-polymer-based nanoparticle conjugated with bevacizumab mAb for the diagnosis of GIST for CT imaging, however still relies significantly on the EPR effect for high-contrast imaging.[39] Our results have indicated that an

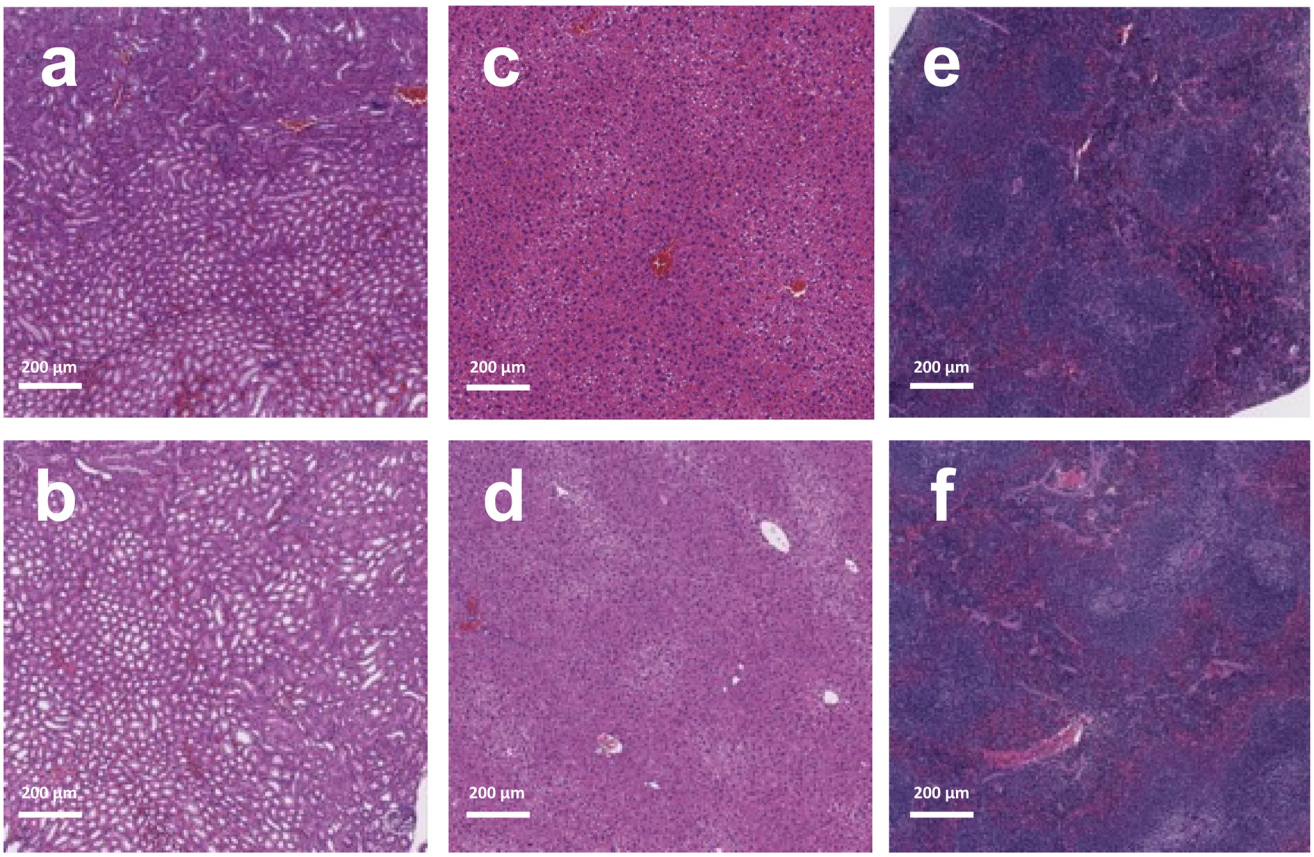

Fig. 7 Histopathology of extracted organs 5 hours following injection of nanoparticles. No significant differences were observed between the control group that received PBS and the test group. H&E staining of major organs after 5 h of pSiNP construct circulation (10 mg kg^{-1} pSiNP, 8 ng kg^{-1} of Aptamer, 198 μg kg^{-1} of silane) in healthy nu/nu mice; (a & b) Kidney, (c & d) Liver, (e & f) Spleen (scale bar = 200 μm). The top row of images were PBS injected mice while the bottom row was pSiNP-NH_2-Cy5.5-PEG-KIT injected mice. Histological analysis showed no major differences between the two sets or organs (Table S3, ESI†).

active-targeted approach for the imaging of GIST using KIT-specific aptamers and pSiNPs can be very effective for *in vivo-based* applications. The high stability and specificity, small size, versatile functional groups, and low-cost of KIT-specific aptamers provide a useful targeting moiety towards GIST compared to KIT mAb and peptides. More specifically, these results have indicated a very versatile platform for both diagnostic and therapeutic-based applications. The porous nature of pSiNPs can enable the loading of various imaging agents and therapeutics, from fluorophores to radiotracers, oligonucleotide payloads, and small-molecule drugs, while the facile conjugation of aptamers can open the door for this nanosystem to be used for various other hard-to-target cancers.

Experimental

Materials

Highly doped p-type doped p^{++}-type (B-doped) crystalline silicon wafers (~0.001 Ω cm resistivity, 100 mm diameter, 525 μm thickness) polished on the (100) face were purchased from Siltronix Corp. All reagents were used as received and purchased from Aldrich Chemicals, Inc. DMDASCO, 2,2-dimethoxy-1,6-diaza-2-silacyclooctane was purchased from Gelest, Inc. Maleimide-PEG-succinimidyl valerate (MAL-PEG-SVA) was purchased from Laysan Bio Inc. All buffer salts were purchased from Gibco Inc. The anti-KIT DNA aptamer was purchased from Integrated DNA Technologies, following the 77 base-long binding regions following 5′-/5AmMC12/GAGGCATACCAGCTT ATTCAAGGGGCCGGGGCAAGGGGGGGGTACCGTGGTAGGACA TAGTAAGTGCAATCTGCGAA-3′. The aptamers were purchased with a 5′-thiol modifier, and one specific batch contained a 3′ 6-FAM fluorophore conjugation. 5-week-old nude mice were purchased from The Jackson Laboratory. Fluorophores were purchased from Lumiprobe. All other chemicals and media were purchased from Sigma and used as is.

Preparation of porous silicon nanoparticles (pSiNP)

pSiNPs were prepared using a previously published "Perforated Etch" method as described previously.[18,26] A highly doped p^{++}-type crystalline silicon wafer (~0.001 Ω cm resistivity, 100 mm diameter, 525 μm thickness, Siltronix, Inc.) was electrochemically etched in an electrolyte solution consisting of 3 : 1 (v : v) of 48% aqueous hydrofluoric acid (HF): to ethanol. (CAUTION: HF is highly toxic and can cause severe burns on contact with the skin or eyes.) Prior to the preparation of the porous layer, the wafer was cleaned using a "sacrificial etch" consisting of etching a thin, porous layer into the wafer (400 mA cm^{-2} applied for 40 s) in the same electrolyte solution. The wafer was subsequently rinsed with ethanol and the porous layer was dissolved in a strong base (2M aqueous KOH). The cell was then rinsed with water and ethanol, before a fresh solution of 3 : 1 HF : ethanol electrolyte solution was added to prepare the nanoparticles. The etching waveform for the particles was generated using LabView (National Instruments, Inc.), and the current was provided by a Keithley 2651A Sourcemeter power supply which was interfaced to LabView. The waveform used was composed of a square wave where a lower 46 mA cm^{-2} current density was applied for 1.818 s, followed by a higher 365 mA cm^{-2} current density pulse for 0.363 s. This waveform was repeated for 200 cycles, generating a thick, porous silicon film with thin regions of high porosity "perforations" that repeat approximately ever 200 nm through the porous layer. The electrolyte solution was subsequently removed, and the porous layer was washed three times with ethanol. This film was then removed from the silicon wafer through a "lift-off" with the application of a constant current density of 3.4 mA cm^{-2} for 180 s in a 1 : 20 (v : v) 48% aqueous HF: ethanol electrolyte solution. The wafer was carefully transferred to a vial filled with deionized water and fragmented into nanoparticles by ultrasonication overnight in a ultrasonication bath. The resulting sonication yielded pSiNPs with an average diameter of 156.3 ± 6.5 as measured by dynamic light scattering (Z-average, intensity based, Zetasizer, Zs90, Malvern Instruments). Following this, the pSiNPs were centrifuged and resuspended in 100% ethanol for storage.

Surface modification of porous silicon nanoparticles

To track the porous silicon nanoparticles, two sets of fluorophores were used, FITC for the *in vitro* experiments and near-IR Cy5.5 dye for *in vivo* experiments. The surface of the nanoparticles were modified with a cyclic azasilane reagent (DMDASCO, 2,2-dimethoxy-1,6-diaza-2-silacyclooctane), which generated primary amine groups on the particle surface *via* a ring-opening click reaction.[8] The azasilane reagent enabled the attachment of fluorophores and an overcoating of polyethylene glycol (MAL-PEG-SVA) to enable the conjugation of ssDNA aptamer constructs as well as to improve the circulation of the particles. For the azasilane attachment, pSiNPs in ethanol were centrifuged (15 000 rpm, 10 min), and the pSiNP pellet was washed in dimethyl sulfoxide (DMSO) to remove protic solvents. Once washed, the nanoparticles (1 mg) were suspended in 400 μL of DMSO and an aliquot of cyclic-silane reagent (100 μL) was added. The pSiNP–silane mixture was allowed to mix for 3 hours. The resulting mix of particles was then washed and centrifuged 3 times with DMSO and finally resuspended in ethanol.

Loading of fluorophores to porous silicon nanoparticles

Two specific fluorophores, NHS Ester-FITC and NHS Ester-Cy5.5 were used as imaging tags for the porous silicon nanoparticles. The fluorophores were bound to the amine-terminated surface of the silane-modified particles. Briefly, 10 μL of 5 mg mL^{-1} of fluorophore dissolved in DMSO was added to 1 mg mL^{-1} of NH_2-terminated particles. The fluorophore was allowed to mix with the particles overnight, free from light. The particles were washed 3 times with ethanol and centrifuged (15 000 rpm, 10 min) to remove any free fluorophore. Fluorophore binding efficiency was measured at 67.5% through UV-Vis fluorescence (Fig. S4a, ESI†). The particles were then dispersed in ethanol and stored in dark.

Attachment of Poly-Ethylene Glycol (PEG) to porous silicon nanoparticles

0.5 mg of the fluorophore-conjugated particles were then dispersed in 80 μL of ethanol and were mixed with a solution of (180 μL) of the heterofunctional linker maleimide-PEG-succinimidyl valerate (MAL-PEG-SVA, MW = 3400, Laysan Bio Inc.) in ethanol (5 mg mL^{-1}) following previous methods.[15] The PEG–nanoparticle mixture was incubated overnight at room temperature under mild shaking and free from light, to prevent bleaching of the fluorophore. Any unbound PEG was removed with a triplicate wash in ethanol and centrifuged (15 000 rpm, 10 min). The particles were then dispersed in ethanol and stored in dark.

Attachment of DNA aptamer ligands to porous silicon nanoparticles

For aptamer conjugation, a concentration of 3.4 mg mL^{-1} of particles were redispersed in DI water. Following this, 0.1 mg of the PEGylated particles were dispersed in a volume of 150 μL of DI water. After, 100 μL of aptamer (100 μM) that was pre-dispersed in DI water, following IDT protocols, was added to the nanoparticle solution. The particle–aptamer mixture was allowed to mix at 4 °C for 2 hours and in dark. The particles were then washed 3 times with DI water and centrifuged (15 000 rpm, 10 min) to remove any unbound aptamer and were resuspended in PBS for immediate use (within 1–2 hours) for *in vitro* cell incubation or *in vivo* injection.

Characterization of porous silicon nanoparticles

Both the hydrodynamic diameter and the ζ-potential measurements were obtained on a Zetasizer, Zs90 (Malvern Instruments). Subsequent pSiNP size measurements were taken with particles dispersed in Dulbecco phosphate-buffer saline (DPBS), pH 7.4, while ζ-potential measurements were measured with particles dispersed in ethanol. The FTIR spectra of the particles were obtained by a Thermo Scientific Nicolet 6700 FTIR instrument fitted with a Smart iTR diamond ATR fixture. TEM images were obtained using a JEOL 1400 plus electron microscope (JEOL USA, Inc.) at 80KeV and subsequently imaged with a Gatan Oneview camera (Gatan, Inc.). Thermogravimetric analysis (TGA) data were obtained using a TA Instruments™ Discovery SDT 650™. Nanoparticle samples were heated from 100 °C–800 °C at a ramp rate of 10 °C min^{-1} in nitrogen. Both weight (%) change and derivative heat flow values were assessed. Dye-loaded particle constructs were assessed using a Molecular Devices™ SpectraMax® iD5 Multi-Mode Microplate Reader. N_2 adsorption/desorption isotherms were obtained using dry nanoparticles at a temperature of 77 K using a Micromeritics ASAP 202 instrument.

Cell culture

GIST-T1 cell lines were obtained from T. Taguchi (Kochi Medical School, Nankoku, Japan), and the human mast cell line HMC 1.2 were obtained from I. Pass, Sanford Burnham Prebys Medical Discovery Institute, San Diego, CA. Both the cell lines were cultured following previous methods.[10] The GIST-T1 cell line was grown in Dulbecco's modified Eagle's medium (DMEM) with 10% FBS, 1% penicillin/streptomycin (Sigma), and 2 mmol L^{-1} glutamine (Sigma). The human mast cell line HMC 1.2 were cultured in Iscove's modified Dulbecco's Medium (Gibco) with 10% FBS, 1% penicillin/streptomycin, and 1.2 mmol L^{-1} 1-Thioglycerol (Sigma).[10]

***In vitro* toxicity.** Cellular viability of cells following nanoparticle treatment, was evaluated by using CCK8 assay kit purchased from Abcam. Then, RAW264.7 macrophage cells were grown in DMEM media supplemented with FBS (10%) and PenStrep (1%), and it was seeded in a 96-well plate (10^4 cells per well) and stored in the incubator in the presence of CO_2 (5%) at 37 °C overnight. To measure *in vitro* toxicity, the cells were incubated with various concentrations of nanoparticles, ranging from 0.03125 mg per 100 μL to 0.5 mg per 100 μL for 48 hours. Following this, all buffer solution was removed, and the cells were washed in triplicates with PBS. Next, WST-8/CCK8 solution was added directly to the cells following manufacturers' protocols, and the cells were allowed to incubate for 2 hours. The absorbance of the cells at 460 nm was subsequently measured using a PerkinElmer LS55 UV-Vis Spectrometer.

***In vitro* flow cytometry experiments and confocal microscopy.** HMC-1.2 cells were kept in suspension, and approximately 1×10^6 cells were isolated and subsequently resuspended in a cold DPBS buffer. Aptamer-conjugated pSiNPs were then incubated with the cells for 1 hour at 4 °C. The cells were then washed thrice with DPBS and resuspended in a DPBS buffer for flow cytometry analysis.

GIST-T1 cells, approximately 1×10^6, were harvested from the cell cultures using trypsin Accutase (Sigma-Aldrich) and were subsequently washed in a cold DPBS buffer. Aptamer-conjugated pSiNPs were then incubated with the cells for 1 hour at 4 °C. The cells were then triplicated, washed with DPBS, and resuspended in a DPBS for flow cytometry analysis (BD Accuri C6). PE anti-human c-KIT antibody (Clone 104D2, BioLegend) was applied in 1:20 dilution for cell staining and as a control. All flow cytometry data were analyzed using FlowJo software.

HMC-1.2 and GIST-T1 cells, approximately 1×10^6 of each, were plated on glass bottom wells and cultured to 50% confluency. Once achieved, the cells were washed three times with PBS and incubated with aptamer-conjugated pSiNPs and free aptamer constructs for 1 hour at 4 °C. The cells were subsequently fixed in 4% paraformaldehyde (Thermo Fisher Scientific), washed, and counter-stained with DAPI (1 : 50 000, Thermo Fisher Scientific) to ensure cell staining.

Establishing the spleen-to-liver GIST metastasis model

Five-week-old male nude mice were purchased from The Jackson Laboratory (Bar Harbor). A mixture of GFP-conjugated T1 (5×10^6 cells) and CAFs (1×10^6 cells), were suspended in 50 μL of Hanks' Balanced Salt Solution (HBSS). After the mice were anesthetized with isoflurane gas, ~1 cm incisions were made in the left abdominal flank, and the cells were injected into the spleen. After 3 weeks, all mice were analyzed using the

IVIS imaging system, and the signals were graphed by total photon flux (p s^{-1}). All animal experiments were conducted and approved in accordance with the Animal Care Committee of the University of California, San Diego (S11020).

***In vivo* experiments.** *in vivo* imaging was performed on GIST-T1-GFP-induced mice. Prior to injection, the mice were weighed, and a concentration of 10 mg kg^{-1} of particles (pSiNP-NH_2-Cy5.5-PEG-KIT, pSiNP-NH_2-Cy5.5-PEG-SCR, and pSiNP-NH_2-Cy5.5-PEG) per mouse was measured out. The mice were subsequently anesthetized using isoflurane gas, and the mice were imaged before particle injection as a control using the IVIS. Cy5.5 signals were measured. Once the preliminary IVIS images were completed, the mice were anesthetized once more, and particles were then subsequently injected *via* tail-vein injection. Immediately, the mice's abdomen was imaged to measure the Cy5.5 signals. This process was repeated for all the mice with the respective control particles (pSiNP-NH_2-Cy5.5-PEG-SCR and pSiNP-NH_2-Cy5.5-PEG). Subsequently, every hour for five, the mice were anesthetized and imaged for the Cy5.5 signals to monitor the intensity and distribution of the particles within the abdomen, particularly the region where the liver, spleen, and kidneys are located. After 5 hours, the mice were sacrificed following university protocols. Blood was collected for toxicity analysis. In addition, the organs of interest, the liver, spleen, and kidneys, were harvested for further *ex vivo* imaging and histology analysis.

***Ex vivo* imaging.** Five hours following the tail-vein injection of the nanoparticle constructs, the liver spleen, and kidneys of the mice were harvested for further IVIS imaging. The images of the isolated organs were named *ex vivo* imaging for the purpose of this study. Following the sacrifice of mice and the harvesting of the organs, all of the liver, spleen, and kidneys were immediately washed with PBS buffer to remove excess blood. The organs were immediately imaged by IVIS to measure both Cy5.5 signals of the internalized particles and GFP signals from tumor metastases on the surface of the organs. This was repeated for the sets of organs for all the mice and the respective controls. GFP and Cy5.5 signals were imaged separately for ImageJ processing to assess signal overlap and GFP co-localization.

***In vivo* toxicity and histology studies.** Nanoparticle toxicity was assessed through blood toxicity using an Alanine aminotransferase (ALT) assay obtained from Sigma. Blood was collected 5 hours after nanoparticle administration from mice post *in vivo* experiments after the mice were sacrificed. The blood was immediately centrifuged at 4000 RPM for 5 minutes to separate serum for ALT assay quantification. The serum from each of the mice's blood samples was separated. Following the manufacturer's protocol, ALT activity was measured utilizing serum samples from each mouse. Control serum samples with PBS-injected mice were utilized as a comparison.

Histological analysis was examined on the mice's liver, spleen, and kidneys post *ex vivo* imaging. Briefly, the organs were washed in PBS buffer and immediately transferred into labelled tissue cassettes before being immersed in a fixative solution, 10% Neutral buffered formalin (NBF) (Sigma), for 24 hours. Following this, the tissue cassettes were subsequently transferred into 70% ethanol for long-term storage. The tissue cassettes were then submitted to UCSD Moores Cancer Center Histology Core for tissue sectioning, plating, and H&E staining. All pathological analyses were completed by Dr Valeria Estrada, MD, from the Histology Core Facility.

Liver section imaging

Once liver samples were imaged *ex vivo*, the samples were subsequently sectioned to assess nanoparticle co-localization to GFP-labeled metastases. Immediately after imaging, liver samples were washed in PBS and placed embedded in Tissue-Tek O.C.T. Compound (Sakura) and immediately frozen. The tissue samples were kept in the dark at −20 °C until submitted to UCSD Moores Cancer Center Histology Core for tissue sectioning and plating. Following this, plated liver sections were imaged using a Keyence BZ-X710, where GFP and Cy5.5 signals were measured. GFP and Cy5.5 signals were imaged separately for ImageJ processing to assess signal overlap and GFP co-localization.

Image analysis

All IVIS images were subsequently modified to remove all background noise using the IVIS proprietary software, PerkinElmer Living Image. For all Cy5.5 signals for *in vivo* images, Radiance (p s^{-1} cm^{-2} sr^{-1}) was assessed to a color scale from 1.50×10^8 to 3.30×10^8 (p s^{-1} cm^{-2} sr^{-1}) to isolate the highest signals within the mouse abdomen, regions where the liver, spleen, and kidney are physiologically located. These regions of interest were isolated to measure the total radiance value for each mouse at each respective time period and were plotted to measure the signal decay over time. For all *ex vivo* images, the Cy5.5 signals were modified to a radiance scale from 5.19×10^8 to 1.32×10^9 (p s^{-1} cm^{-2} sr^{-1}), and GFP signals were modified from 1.95×10^8 to 7.66×10^9 (p s^{-1} cm^{-2} sr^{-1}). Cy5.5 and GFP signals of the organs were imaged separately.

To analyze the co-localization of Cy5.5 and GFP signals, the normalized images were overlaid using ImageJ, and the signals from both Cy5.5 and GFP images were merged. The overlap of Cy5.5 signal to total GFP signals enabled a quantitative value to calculate the signal overlap. The following equation was used to calculate GFP co-localization: $$\text{GFP Co-localization } (\%) = \frac{\text{Total Merged Signal}}{\text{Total GFP Signal}} \times 100.$$ All co-localization calculations were only assessed within the imaged area of the tumor. Any Cy5.5 signal associated with the nanoparticle constructs that did not merge with the visible GFP signals from the organs was assumed to not bind with the GIST-T1 metastases. This same analysis was utilized for the frozen liver tissue section images where Cy5.5 and GFP signals were measured.

Statistical analysis

All statistical analyses were assessed using GraphPad Prism 9. The investigators were not blinded throughout *in vivo* experiments or outcome assessment, except for the pathological

assessments of tissues by Dr Valeria Estrada, MD. Statistical significance was determined by two-tailed unpaired Student's *t*-test with Welch correction and one-way ANOVA for multiple comparisons when deemed appropriate.

Conclusions

In summary, porous silicon nanoparticles decorated with anti-KIT DNA aptamers showed highly effective labelling of human GIST cells in a clinically relevant GIST liver metastasis model. This diagnostic platform showed clear multivalency effects relative to free KIT aptamers for targeting *in vitro* and highly effective in *in vivo* and *ex vivo* targeting of GIST metastases in RES and MPS clearance tissues, the liver, and spleen. The increased efficacy of tumor cell homing was attributed to the multivalent interactions that result from attaching multiple aptamer-targeting agents to a single nanoparticle. While this study focused on an imaging/diagnostic application, the results have implications for use of the aptamer-pSiNP system as a delivery vehicle for therapeutics.

Conflicts of interest

MJS is a scientific founder (SF), a member of the Board of Directors (BOD), Advisory Board (AB), Scientific Advisory Board (SAB), acts as a paid consultant (PC), or has an equity interest (EI) in the following: Aivocode, Inc (AB, EI); Bejing ITEC Technologies (SAB, PC); Cend Therapeutics (SF, BOD, EI); Illumina (EI), Matrix Technologies (EI); NanoVision Bio (SAB, EI); Quanterix (EI), Spinnaker Biosciences, Inc. (SF, BOD, EI); TruTag Technologies (SAB, EI); and Well-Healthcare Technologies (SAB, PC). MJS is also a Guest Professor at Zhejiang University, China. Although one or more of the grants that supported this research has been identified for conflict-of-interest management based on the overall scope of the project and its potential benefit to the above companies, the research findings included in this particular publication may not necessarily relate to their interests. The terms of this arrangement have been reviewed and approved by the University of California, San Diego in accordance with its conflict-of-interest policies.

Acknowledgements

The authors acknowledge the use of facilities and instrumentation supported by the National Science Foundation through the UC San Diego Materials Research Science and Engineering Center (UCSD MRSEC) DMR-2011924 and by the San Diego Nanotechnology Infrastructure (SDNI) of UCSD, a member of the National Nanotechnology Coordinated Infrastructure, which is supported by the National Science Foundation Grant ECCS-1542148. The authors also would like to thank the University of California, San Diego – Cellular and Molecular Medicine Electron Microscopy Core (UCSD-CMM-EM Core, RRID: SCR_022039) for equipment access and technical assistance. The UCSD-CMM-EM Core is partially supported by the National Institutes of Health Award number S10OD023527. The authors thank UCSD's Altman Clinical and Translational Research Institute (ACTRI) for the 2020 Pilot Project Grant (P. R.), National Institutes of Health Grant UL1TR001442. In addition, S.V. acknowledges support from UCSD's Chancellor's Interdisciplinary Collaboratories as well as the Natural Sciences and Engineering Research Council of Canada Postgraduate Scholarship – Doctoral program (NSERC PGS-D).

References

1 G. L. Ma, J. D. Murphy, M. E. Martinez and J. K. Sicklick, *Cancer Epidemiol. Biomarkers Prev.*, 2015, **24**, 298–302.
2 Y. N. Kang, H. R. Jung and I. Hwang, *Cancer Res. Treat.*, 2010, **42**, 135–143.
3 C. L. Corless, C. M. Barnett and M. C. Heinrich, *Nat. Rev. Cancer*, 2011, **11**, 865–878.
4 C. M. Barnett, C. L. Corless and M. C. Heinrich, *Clin. Oncol.*, 2013, **27**, 871–888.
5 C. A. Metildi, C. M. Tang, S. Kaushal, S. Y. Leonard, P. Magistri, H. S. Tran Cao, R. M. Hoffman, M. Bouvet and J. K. Sicklick, *Ann. Surg. Oncol.*, 2013, **20**(Suppl 3), S693–700.
6 C. Tuerk and L. Gold, *Science*, 1990, **249**, 505–510.
7 A. D. Ellington and J. W. Szostak, *Nature*, 1990, **346**, 818–822.
8 D. Kim, J. M. Zuidema, J. Kang, Y. Pan, L. Wu, D. Warther, B. Arkles and M. J. Sailor, *J. Am. Chem. Soc.*, 2016, **138**, 15106–15109.
9 P. Ray, K. D. Viles, E. E. Soule and R. S. Woodruff, *Arch. Immunol. Ther. Exp.*, 2013, **61**, 255–271.
10 S. Banerjee, H. Yoon, M. Yebra, C.-M. Tang, M. Gilardi, J. S. Shankara Narayanan, R. R. White, J. K. Sicklick and P. Ray, *Mol. Cancer Ther.*, 2020, **19**, 1173.
11 H. Kang, W. R. Stiles, Y. Baek, S. Nomura, K. Bao, S. Hu, G. K. Park, M. J. Jo, H. I, J.-L. Coll, B. P. Rubin and H. S. Choi, *Adv. Mater.*, 2020, **32**, 1905899.
12 J. Tan, N. Yang, L. Zhong, J. Tan, Z. Hu, Q. Zhao, W. Gong, Z. Zhang, R. Zheng, Z. Lai, Y. Li, C. Zhou, G. Zhang, D. Zheng, Y. Zhang, S. Wu, X. Jiang, J. Zhong, Y. Huang, S. Zhou and Y. Zhao, *Theranostics*, 2017, **7**, 4862–4876.
13 D. Kim, J. Kang, T. Wang, H. G. Ryu, J. M. Zuidema, J. Joo, M. Kim, Y. Huh, J. Jung, K. H. Ahn, K. H. Kim and M. J. Sailor, *Adv. Mater.*, 2017, **29**, 1703309.
14 J. Kang, D. Kim, J. Wang, Y. Han, J. M. Zuidema, A. Hariri, J.-H. Park, J. V. Jokerst and M. J. Sailor, *Adv. Mater.*, 2018, **30**, 1800512.
15 A. Bertucci, K.-H. Kim, J. Kang, J. M. Zuidema, S. H. Lee, E. J. Kwon, D. Kim, S. B. Howell, F. Ricci, E. Ruoslahti, H.-J. Jang and M. J. Sailor, *ACS Appl. Mater. Interfaces*, 2019, **11**, 23926–23937.
16 J. Kang, J. Joo, E. J. Kwon, M. Skalak, S. Hussain, Z.-G. She, E. Ruoslahti, S. N. Bhatia and M. J. Sailor, *Adv. Mater.*, 2016, **28**, 7962–7969.

17 B. Kim, S. Sun, J. A. Varner, S. B. Howell, E. Ruoslahti and M. J. Sailor, *Adv. Mater.*, 2019, **31**, 1902952.
18 M. J. Sailor, *Porous Silicon in Practice: Preparation, Characterization, and Applications*, Wiley-VCH, Weinheim, Germany, 2012.
19 L. Gu, L. E. Ruff, Z. Qin, M. Corr, S. M. Hedrick and M. J. Sailor, *Adv. Mater.*, 2012, **24**, 3981–3987.
20 F. Chen, H. Hong, Y. Zhang, H. F. Valdovinos, S. Shi, G. S. Kwon, C. P. Theuer, T. E. Barnhart and W. Cai, *ACS Nano*, 2013, **7**, 9027–9039.
21 E. Secret, K. Smith, V. Dubljevic, E. Moore, P. Macardle, B. Delalat, M.-L. Rogers, T. G. Johns, J.-O. Durand, F. Cunin and N. H. Voelcker, *Adv. Healthcare Mater.*, 2013, **2**, 718–727.
22 A. P. Mann, P. Scodeller, S. Hussain, J. Joo, E. Kwon, G. B. Braun, T. Mölder, Z.-G. She, V. R. Kotamraju, B. Ranscht, S. Krajewski, T. Teesalu, S. Bhatia, M. J. Sailor and E. Ruoslahti, *Nat. Commun.*, 2016, **7**, 11980.
23 B. Kim, J.-H. Park and M. J. Sailor, *Adv. Mater.*1903637.
24 F. Zhang, A. Correia, E. Mäkilä, W. Li, J. Salonen, J. J. Hirvonen, H. Zhang and H. A. Santos, *ACS Appl. Mater. Interfaces*, 2017, **9**, 10034–10046.
25 M. Terracciano, I. Rea, N. Borbone, R. Moretta, G. Oliviero, G. Piccialli and L. De Stefano, *Molecules*, 2019, **24**(12), 2216.
26 Z. Qin, J. Joo, L. Gu and M. J. Sailor, *Part. Part. Syst. Charact.*, 2014, **31**, 252–256.
27 S. Banerjee, H. Yoon, S. Ting, C.-M. Tang, M. Yebra, A. T. Wenzel, H. Yeerna, J. P. Mesirov, R. J. Wechsler-Reya, P. Tamayo and J. K. Sicklick, *Mol. Cancer Ther.*, 2021, **20**, 2035–2048.
28 J. K. Sicklick, S. Y. Leonard, M. L. Babicky, C.-M. Tang, E. S. Mose, R. P. French, D. V. Jaquish, C. K. Hoh, M. Peterson, R. Schwab and A. M. Lowy, *J. Transl. Med.*, 2014, **12**, 41.
29 M. Yebra, S. Bhargava, A. Kumar, A. M. Burgoyne, C.-M. Tang, H. Yoon, S. Banerjee, J. Aguilera, T. Cordes, V. Sheth, S. Noh, R. Ustoy, S. Li, S. J. Advani, C. L. Corless, M. C. Heinrich, R. Kurzrock, S. M. Lippman, P. T. Fanta, O. Harismendy, C. Metallo and J. K. Sicklick, *Clin. Cancer Res.*, 2022, **28**, 187–200.
30 H. Yoon, C.-M. Tang, S. Banerjee, M. Yebra, S. Noh, A. M. Burgoyne, J. D. l. Torre, M. D. Siena, M. Liu, L. R. Klug, Y. Y. Choi, M. Hosseini, A. L. Delgado, Z. Wang, R. P. French, A. Lowy, R. P. DeMatteo, M. C. Heinrich, A. A. Molinolo, J. S. Gutkind, O. Harismendy and J. K. Sicklick, *Oncogene*, 2021, **40**, 1957–1973.
31 S. E. A. Gratton, P. A. Ropp, P. D. Pohlhaus, J. C. Luft, V. J. Madden, M. E. Napier and J. M. DeSimone, *Proc. Natl. Acad. Sci. U. S. A.*, 2008, **105**, 11613–11618.
32 G. Thurston, J. W. McLean, M. Rizen, P. Baluk, A. Haskell, T. J. Murphy, D. Hanahan and D. M. McDonald, *J. Clin. Invest.*, 1998, **101**, 1401–1413.
33 N. Billinton and A. W. Knight, *Anal. Biochem.*, 2001, **291**, 175–197.
34 E. McCormack, D. R. Micklem, L.-E. Pindard, E. Silden, P. Gallant, A. Belenkov, J. B. Lorens and B. T. Gjertsen, *Mol. Imaging*, 2007, **6**, 7290.
35 B. Kim, H.-B. Pang, J. Kang, J.-H. Park, E. Ruoslahti and M. J. Sailor, *Nat. Commun.*, 2018, **9**, 1969.
36 J.-H. Park, L. Gu, G. von Maltzahn, E. Ruoslahti, S. N. Bhatia and M. J. Sailor, *Nat. Mater.*, 2009, **8**, 331–336.
37 Y. Li, Z. Liu, L. Li, W. Lian, Y. He, E. Khalil, E. Mäkilä, W. Zhang, G. Torrieri, X. Liu, J. Su, Y. Xiu, F. Fontana, J. Salonen, J. Hirvonen, W. Liu, H. Zhang, H. A. Santos and X. Deng, *Adv. Sci.*, 2020, **7**, 2001129.
38 M. Tanaka, H. Kataoka, S. Yano, H. Ohi, K. Moriwaki, H. Akashi, T. Taguchi, N. Hayashi, S. Hamano, Y. Mori, E. Kubota, S. Tanida and T. Joh, *Mol. Cancer Ther.*, 2014, **13**, 767–775.
39 T. B. Ligiero, C. Cerqueira-Coutinho, M. de Souza Albernaz, M. Szwed, E. S. Bernardes, M. A. V. Wasserman and R. Santos-Oliveira, *Biomed. Phys. Eng. Express*, 2016, **2**, 045017.